# Fully resolved Zeeman pattern in the Stern-Gerlach deflection spectrum of $O_2$ ($^3\Sigma_g^-$, $K=1$)

N. A. Kuebler, M. B. Robin, J. J. Yang,*, and A. Gedanken†
*AT&T Bell Laboratories, Murray Hill, New Jersey 07974*

D. R. Herrick
*Department of Chemistry, University of Oregon, Eugene, Oregon 97403*
(Received 12 February 1988)

The Stern-Gerlach magnetic deflection spectrum of a molecular beam of $^{16}O_2$ cooled by supersonic expansion to its lowest rotational level ($K=1$) reveals nine spatially separated peaks within a span of 2 cm. These peaks readily are assigned from a calculation of the Zeeman energies of the $K=1$ spin-rotation sublevels characterized by $M_J$, and the assumption of a uniform field gradient within the deflecting magnet gap. However, the variable widths of the observed peaks and the decreasing deflection of certain $M_J$ peaks with increasing field above 14 kG require the explicit consideration of field-gradient inhomogeneities. The theory for this is developed and the spectral profiles again computed with field-gradient inhomogeneity and rotational temperature ($T_{rot}$) as variables. Agreement of the theoretical shifts, bandwidths, and relative intensities with increasing field gradient when compared with the experimental spectra is very good, and $T_{rot}$ is found to be 3.5 K. The deflection spectrum of a beam of $^{17}O_2$ differs from that of $^{16}O_2$, reflecting the population of the $K=0$ rotational level in the $^{17}O_2$ isotopomer. The oxygen dimer and trimer appear to be paramagnetic, but this result is tentative.

## I. INTRODUCTION

Although the Stern-Gerlach experiment eventually won the Nobel prize[1] and remains a classic textbook example, very little of chemical interest has been done with it in the 60 years since it appeared. In the original Stern-Gerlach experiment,[2-6] an effusive beam of Ag atoms in their $^2S_{1/2}$ ground state traverses a region of inhomogeneous magnetic field, and the electron-spin magnetic moment of the atom interacts with the field gradient both to reorient the moment and to displace the atom laterally. This displacement is either in the up-field direction or in the down-field direction, depending upon the relative orientations of the magnetic moment and the direction of the field gradient. According to classical theory, the random orientations of the magnetic moments with respect to the direction of the field gradient will lead to a spatially broadened but unshifted beam profile. In contrast, quantum mechanics predicts that all atoms in the otherwise random beam upon entering the field will align their moments either parallel or antiparallel to the field, resulting in two spin-polarized beams separated in space. Stern and Gerlach observed that after a flight of a few centimeters through the magnetic field gradient, the atomic beam of silver was split into two components with a spatial separation of $\sim 0.1$ mm.

At the time, the Stern-Gerlach result was hailed as illustrating several interesting aspects of quantum mechanics, while at the same time using a chemically uninteresting species. With the quantum mechanics now firmly established, one would hope to be able to reverse the emphasis and thereby apply the Stern-Gerlach technique to the study of molecular species which are chemically interesting. In particular, the technique could be of great use in studying the magnetic properties of transient molecules or of short-lived states of more permanent molecules. In fact, a few attempts recently have been made in this direction using molecular beams seeded with metallic clusters.[7-11] Though successful in their way, these experiments only revealed splitting due to unpaired electron spin in the clusters. We report here the Stern-Gerlach deflection spectra of the paramagnetic $O_2$ molecule. Though not as inherently challenging as working with beams of metal clusters, this work on $O_2$ shows for the first time how important spin-rotation interaction can be in this type of spectroscopy.

In addition to the spatially resolved Stern-Gerlach experiments of others on the electron spin of metal clusters, seeded-beam experiments related to these have been reported by Amirav and Navon,[12,13] who used a fixed-detector position and studied the attenuation of the molecular-beam signal as the field gradient was applied. They found that not all paramagnetic molecules would deflect in the field gradient, their explanation being that fast intramolecular spin relaxation induced by spin-orbit coupling destroys the magnetic orientation necessary for macroscopic deflection. Amirav and co-workers[14-16] also have used a variant of this fixed-detector spectrometer to monitor rf resonances in beams of alkali-metal atoms and the $O_2$ molecule.

 

## II. EXPERIMENTAL DETAILS

### A. Apparatus and materials

A schematic of the apparatus used in this work is shown in Fig. 1. PV is a pulsed valve (either a Lasertechnics piezoelectric valve or a General Valve Corporation solenoid valve) operating with a nozzle diameter of 100–300 $\mu$m and at stagnation pressures of 200–7000 Torr. The supersonic expansion is skimmed at A1 using a conical skimmer of 1-mm opening. In those cases where the beam was operated in a cw mode, it was chopped (400 Hz) using a Bulova tuning-fork chopper (TF), which was otherwise retracted from the beam path. A2 and A3 are sets of apertures of 4 mm height ($x$) and variable width ($y$) which can be brought onto the beam axis ($x$). The magnetic field gradient is produced with an electromagnet having Fe-Co-V (49%-49%-2%) pole pieces of 5 cm diameter inserted through the vacuum walls. These pole faces (PF1 and PF2) are of the Rabi type, shaped according to the prescription of Kellogg and Millman,[17] as is described further in Sec. II B. The detector (MS) is a quadrupole mass spectrometer having an electron-impact ionizer masked by a $0.25\times4$-mm$^2$ slit. The mass spectrometer is mounted on a bellows feedthrough and its position in the $x$ direction is scanned using a stepping motor (M). The magnetic and detection chambers are separated by a gate valve (GV). Assemblies PV, TF, A2, A3, and MS are mounted on $x,y,z$ translators for alignment purposes. Vacuum is maintained by diffusion pumps P1 (10 in.), P2 (4 in), and P3 (6 in).

In operation, the mass spectrometer is tuned to the beam species of interest and the amplified signal fed to either a boxcar or lockin detector, depending upon whether the valve PV is operated in the pulsed or cw mode. This processed signal is then plotted as the motor M drives the mass spectrometer in the $x$ direction. Because of the residual magnetization of the pole pieces, it was necessary to energize the magnet with a slight negative current in order to record the true "zero-field" deflection pattern. When working with pure $O_2$ in the cw mode with a backing pressure of 1 atm, an undeflected zero-field peak was observed having a width at half height of 0.8 mm.

In addition to working with $^{16}O_2$ (research grade), beam-deflection studies also were carried out using an isotopically enriched sample of $O_2$ containing 36 at. % $^{17}O$ and 64 at. % $^{18}O$. This allowed the independent determination of the deflection spectra of $^{16}O_2$, $^{17}O_2$, $^{17}O^{18}O$, and $^{18}O_2$.

At high stagnation pressures, the mass spectrum of the pulsed beam showed the presence of $O_4$ and $O_6$ or one or more of their precursors. Consequently, deflection spectra also were run with the mass spectrometer tuned to $O_4^+$ and to $O_6^+$.

### B. Magnetic field

The pole faces of our magnet have the standard Rabi configuration in which the field in the gap mimics the "two-wire model,"[17] with wires located at the intersections of two circles at $x=0, y=a$ and $x=0, y=-a$. The Rabi magnet pole faces are constructed such that the radius of the semicircular convex pole face PF1 (Fig. 2) is $a=0.318$ cm, whereas that of the semicircular concave pole face PF2 is $1.25a$. The separation of the pole faces

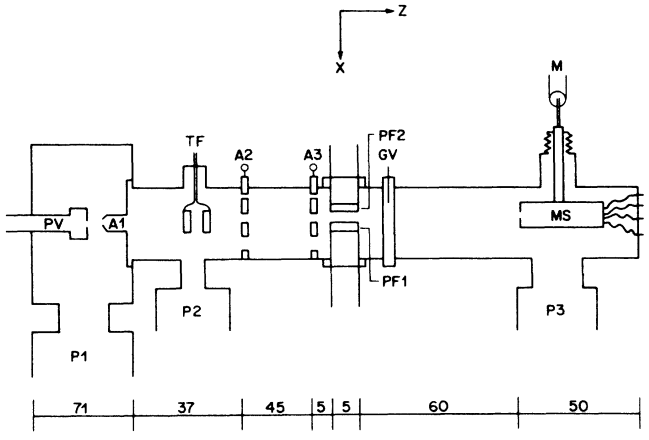


FIG. 1. Schematic diagram of the molecular beam Stern-Gerlach deflection apparatus. PV is a pulsed valve capable of being operated in the cw mode, the output of which is skimmed by skimmer A1 and chopped by tuning fork TF if cw. The beam is further collimated by apertures A2 and A3 before entering the gap between magnet pole faces PF1 and PF2. The gate valve GV separates the magnet from the chamber bearing the mass spectrometer MS, which is translated in the $x$ direction by the stepping motor M. Vacuum is maintained by pumps P1, P2, and P3. The scale at the bottom of the drawing gives the $z$ dimensions of the apparatus in centimeters.

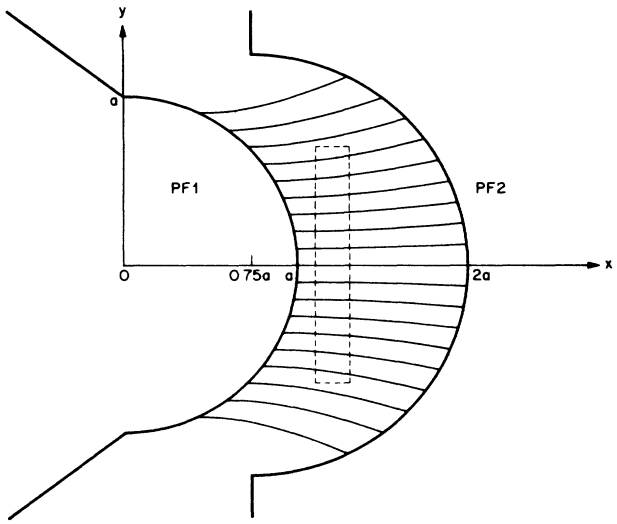


FIG. 2. Details of the gradient magnet constructed according to Kellogg and Millman (Ref. 17); the radius $a$ of PF1 is 3.18 mm. Also shown are the lines of steepest descent of the potential between pole faces PF1 and PF2 as well as the sweet zone as a dotted rectangle. A magnetic molecule at a point within the magnet gap will experience a force along the line of steepest descent passing through that point.

in the $x$ direction is $a$ and the separation between centers of the semicylinders is $0.75a$.

The magnitude of the field in the two-wire model is

$$H=H_0(x_0^2+a^2)/[(x^2+y^2+a^2)^2-4a^2y^2]^{1/2}\ , \qquad (1)$$

where $H_0$ is the value of the field at $x_0=1.2a$, $y=0$. This point is the center of a "sweet zone" defined by the narrow ribbon $1.1a<x<1.3a$ and $-0.7a<y<0.7a$, within which the field gradient in the $x$ direction is nearly constant. The magnetic lines of force in the two-wire model depicting the direction of the force on a magnetic molecule in the magnet gap are shown in Fig. 2, together with the dimensions and orientation of the sweet zone.

If the adiabatic potential energy of a molecule at a point in the field is $E$, then the force on the molecule is

$$F=-\nabla E=-(dE/dH)\nabla H\ . \qquad (2)$$

In such a field, a molecule in a state for which $dE/dH<0$ is deflected toward the convex pole face (in the negative $x$ direction), while a molecule in a state for which $dE/dH>0$ is deflected in the opposite direction. The $y$ component of the force vanishes at the convex pole face. As the lines of force in Fig. 2 suggest, within the sweet zone there will be very little deflection of a molecule in the $y$ direction.

In the theory that follows, we assume a simplified one-dimensional model of the two-wire field in which only deflections in the $\pm x$ direction are considered. Two parameters, $\alpha_0$ and $\beta_0$, which express the local variation of the field, are defined by

$$dH/dx=-\alpha_0 H \qquad (3)$$

and

$$d^2H/dx^2=\alpha_0^2\beta_0 H\ . \qquad (4)$$

In the two-wire field, $\alpha_0=0.984/a$ and $\beta_0=1.15$ at the center of the sweet zone. More generally, we may consider $\alpha_0$ and $\beta_0$ to be empirical parameters for a quadratic field

$$H/H_0=1-\alpha_0(x-x_0)+\alpha_0^2\beta_0(x-x_0)^2/2\ , \qquad (5)$$

which represents an effective field for molecules within the sweet zone. In simulating Stern-Gerlach spectra using Eq. (5), it is found that variation of $\alpha$ results in variation of the deflection amplitude, whereas variation of $\beta$ influences the peak bandwidth.

Field gradients were not measured in our experiment; however, a Hall probe was used to record the field strength at a central point as a function of magnet current. It is presumed [Eqs. (3) and (4)] as a first approximation that the gradients and second derivatives at all points in the gap scale linearly with the field as measured at the Hall probe. Moreover, because the dimensions of our Hall probe were nearly those of the magnet gap itself, the "$H_0$" fields we have measured most likely are somewhat different from those existing at the true center of the sweet zone. Indeed, as will be seen in the following, simulation of the observed Stern-Gerlach patterns shows that the $H_0$ fields as measured using the Hall probe are approximately 10–20 % higher than the best-fit values. Because the field gradient in the gap of the magnet is not homogeneous, it was necessary when running spectra to search the sweet zone empirically for the position of highest homogeneity as judged by the overall resolution of the field-split spectra.

## III. THEORY OF THE $O_2$ DEFLECTION SPECTRUM

### A. Deflections in low fields

The deflection force in the Stern-Gerlach experiment results from the coupling of the net angular momentum of the molecule with the magnetic field gradient through the Zeeman interaction, Eq. (2). In the general polyatomic molecule, there are several possible motions which may contribute to the angular momentum: electron spin, electron orbital motion, nuclear spin, internal rotation, degenerate vibrational motions, and end-over-end rotation of the molecule. Inasmuch as the angular momentum varies inversely with the rotating mass, the moments for electron-spin and electron-orbital motions are several thousand times larger than for any angular momentum involving nuclear motions.[18] Though the resolution of our apparatus is insufficient to resolve the small Stern-Gerlach deflections resulting from the nuclear motions themselves, the nuclear motions nonetheless can become very important when strongly mixed with electronic motions which are characterized by large Stern-Gerlach deflections.

Because rotational angular momentum can be an important factor in the deflection spectrum, it is of great advantage to work initially with molecular beams in which the rotational temperature is as low as possible, so as to limit the number of rotational levels contributing to the spectrum. Supersonic beams are ideal for this experiment because they not only result in a beam of high number density and high spatial collimation, but because such expansions also result in very low rotational temperatures.[19] Earlier supersonic-expansion experiments on oxygen at a stagnation pressure of $\sim 1$ atm show that the rotational temperature in the beam is of the order 5–10 K.[14–16,20]

The standard Stern-Gerlach treatment[6,10] assumes a constant force on the molecule as it passes through the magnetic field. The result is a deflection of

$$\Delta X_i=k_0H_0dE_i/dH \qquad (6)$$

at some point beyond the magnet. In this equation, the subscript $i$ denotes the $i$th molecular state and $H_0$ is the value of the field at the center of the sweet zone; the constant $k_0$ accounts for both the gradient of the field within the zone and several other physical factors in the experiment. Assuming a linear Zeeman effect, $dE_i/dH$ frequently is taken as equal to $g_i\mu_i$, with $g_i$ being the $g$ factor of the $i$th state and $\mu_i$ being the magnetic moment of level $i$ in Bohr magnetons. However, as will be shown in the following, this is a poor assumption for most levels of oxygen. The constant $k_0$ appearing in Eq. (6) may be expressed in terms of the experimental constants as

$$k_0=\alpha_0 G \ , \tag{7}$$

$$G=l(l+2L)/2mv^2 \ , \tag{8}$$

where $l$ is the length of the magnet, $L$ is the distance from the magnet to the detector, and the molecules of mass $m$ move with velocity $v$. Energy is measured in units of $h$, Planck's constant.

As a sample molecule, we choose $O_2$ in its $^3\Sigma_g^-$ ground state. Several previous molecular beam studies on $O_2$ Refs. (14–16 and 20) show that under the conditions used here, there is very strong rotational cooling such that ~98% of the molecules are in the lowest rotational state. Since rotational levels with $K=0,2,4,\ldots$ are forbidden in $^{16}O_2$ and $^{18}O_2$ as a consequence of the nuclear statistics which follow from zero nuclear spins in the $^{16}O$ and $^{18}O$ nuclei, the lowest such level is $K=1$ in these isotopomers. On the other hand, because $^{17}O$ has $I=\frac{5}{2}$, rotational levels appear in $^{17}O_2$ and $^{17}O\,^{18}O$ having both odd and even $K$, with $K=0$ being lowest.

Being very nearly a Hund's case-$b$ system, the rotational angular momentum $K$ in $O_2$ is added vectorially to the electron-spin angular momentum $S=1$ to produce the angular momentum vector $J=K+S$, which equals 0 , 1 , and 2 when $K=1$, as in Fig. 3. It is most likely that there is a thermal equilibrium among the three $J$ levels of $K=1$ in the molecular beam.[20] Each $J$ component has $2J+1$ sublevels $(M_J=+J,\ldots,0,\ldots,-J)$, each with a characteristic Zeeman energy in a magnetic field. The vectors $K$, $S$, and $J$ are the only ones of interest at this point since there are no nuclear moments in $^{16}O_2$ and the $^3\Sigma$ ground state has no orbital momentum.

Figure 3 depicts the Zeeman energies $E_i$ for the sub-

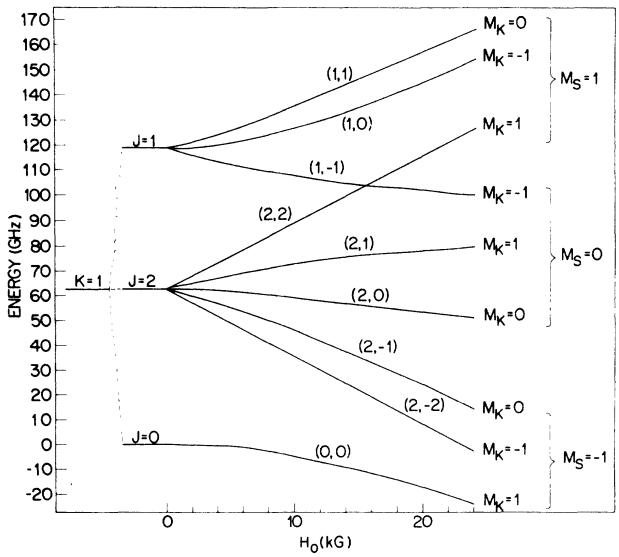


FIG. 3. Combination of the $K=1$ rotational quantum number of oxygen with $S$, the electronic spin quantum number, to produce levels with quantum numbers $J$. In a magnetic field, the $J$ levels are resolved into their $M_J$ sublevels as calculated on the right. Each of the levels is identified as $(J,M_J)$. At fields above 20 kG, the levels tend to regroup so as to go asymptotically to the spin-only values.

states in the $K=1$ manifold of oxygen. The energies were computed by diagonalizing the Zeeman Hamiltonian in a rotational basis including quantum numbers up to $J=20$ using the field-free rotational constants of Tinkham and Strandberg.[21] This Zeeman pattern agrees closely with the unpublished pattern which Tinkham[22] calculated using an effective Hamiltonian. Because the lowest component of the next lowest rotational level ($K=3$, $J=2$) in $^{16}O_2$ is approximately 378 GHz above the uppermost level ($J=1$) of the $K=1$ manifold at zero field, we focus first on the $K=1$ manifold.

Individual Zeeman curves in Fig. 3 are labeled as $(J,M_J)$ at low field. $M_J$ is a good quantum number at all fields, whereas $J$ is appropriate only to the zero-field case. The $M_S$ values indicated at high fields are appropriate to the Paschen-Back limit. In this high-field situation, the internal coupling of $K$ and $S$ is broken by the external field. With $K$ and $S$ then independently coupled to the external field, the result is a set of three levels, each of which is triply near-degenerate. This coarse-grained pattern of three levels is that appropriate to the triplet spin-only case. As the field strength of our magnet at saturation is only 22.6 kG, at the highest fields we are just at the threshold of the Paschen-Back region in regard to the Zeeman pattern. Speaking generally, spin-rotational effects in Stern-Gerlach deflection spectra appear in the field region below the Paschen-Back onset. This in turn is dependent upon the strength of the spin-rotation interaction, a quantity which is quite large in the $^3\Sigma_g^-$ state of $O_2$. At fields far above the Paschen-Back onset, the Stern-Gerlach splitting pattern is essentially that of the paramagnetic nonrotating molecule, except at fields where the spin-rotation interaction can lead to level anticrossing. The high-field deflection patterns are discussed further in Sec. III B.

Using the Zeeman energies depicted in Fig. 3 together with Eq. (6) allows one to convert the energy shifts $E_i$ into spatial deflections, $\Delta X_i$, as in Fig. 4. Again, the curves have been labeled by the quantum numbers $(J,M_J)$. As indicated by Eq. (2), the sign of the Stern-Gerlach deflection of a particular level is dictated by the sign of $dE_i/dH$ at that field. In this paper, we label as "paramagnetic" those levels which deflect toward higher magnetic field, whereas "diamagnetic" levels deflect toward lower field. Note that though the Zeeman levels at high field (24 kG) are just beginning to separate as the Paschen-Back limit is approached (Fig. 3), at the corresponding fields in the Stern-Gerlach spectrum (Fig. 4) the separation as measured by deflection is much further along, with the displacements clustering into a clear triplet pattern at 24 kG. As mentioned in the preceding, each component of this triplet at very high fields is itself an unresolvable triplet when $K=1$.

A particularly interesting feature of the predicted deflection curves, Fig. 4, is the crossing pattern in the 6–16-kG region for the (0,0), (1,−1), and (2,0) states. In contrast, the (2,2) and (2,−2) levels are predicted to show a simple linearity of displacement with increasing field out to 30 kG.

Other views of the Zeeman deflections as predicted by

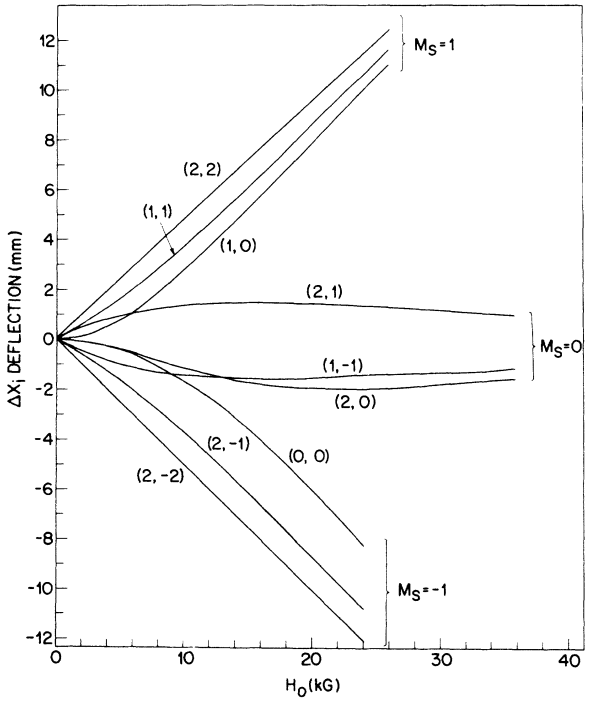


FIG. 4. Calculated deflections of oxygen molecules in the $(J,M_J)$ spin-rotational sublevels of the $K=1$ state. The constant of proportionality $k_0$ between the deflection $\Delta X_i$ and $H_0 dE_i/dH$ was taken as $1.85\times10^{-5}$ cm/MHz, this being the value appropriate to the measured deflection of the (2,2) level at 4 kG.

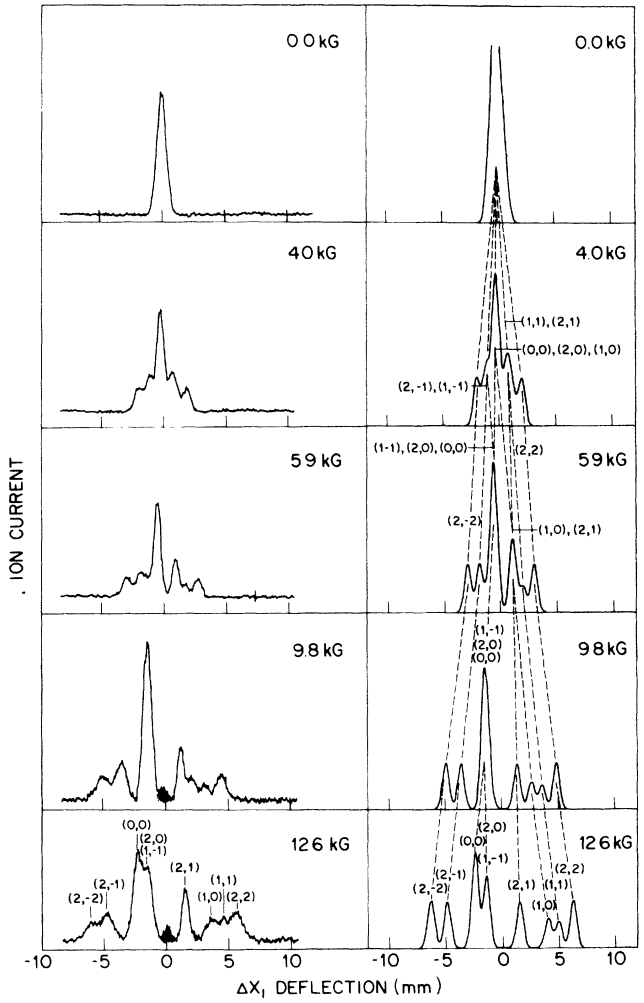


FIG. 5. *Left-panel*: Stern-Gerlach deflection patterns measured for oxygen as a function of field strength $H_0$ (0.0–12.6 kG) in the sweet zone. The oxygen stagnation pressure was 2200 Torr and the nozzle diameter 300 $\mu$m. See text for a discussion of the cross-hatched peak at $\Delta X_i=0$ mm. *Right panel*: Calculated magnetic deflection patterns for oxygen assuming a constant width for each component and thermal equilibrium among the zero-field levels $J=0$, $J=2$, and $J=1$ at 4 K. Levels are labeled as $(J,M_J)$.

Eq. (6) are shown in Figs. 5 and 6, in which each spin-rotational state is represented by a simple Gaussian distribution function, reflecting the lateral spread of molecules at aperture A2, and the convolution with the detector slit function. The assumed signal function for the $i$th state is

$$S_i(X)=[N_i/\Sigma(2\pi)^{1/2}]\exp\{-\tfrac{1}{2}[(X-x_0-\Delta X_i)/\Sigma]^2\}\ , \tag{9}$$

where $\Sigma=0.3$ mm is characteristic of the experimental zero-field signal, and $N_i$ is a rotational Boltzmann distribution factor. A value of $k_0^{\rm expt}=1.85\times10^{-5}$ cm/MHz was chosen as a best-fit value in the low-field linear Zeeman region, and was used for computing these patterns at all fields.

The results in Figs. 5 and 6 are calculated assuming that the $J=0$, 2, and 1 levels at zero field are in thermal equilibrium at a rotational temperature of 4 K; as expected, states with $K=1$ predominate at this temperature. It is implicit in our calculation that since the thermally equilibrated molecules travel at supersonic speeds ($v=730$ m/s), they enter the fringing magnetic field essentially instantaneously. In this case, the sudden approximation applies, and all of the $M_J$ levels for a particular $J$ manifold are populated with equal probability as the molecules enter the field. These calculations do not consider the effects of the velocity distribution within the beam or the possible formation of clusters.

The Stern-Gerlach deflection pattern predicted at low field for $^{16}O_2$ in $K=3$ illustrates a feature not present in the curves for $K=1$. Looking at the $J=2$ and $J=4$ sublevels of the $K=3$ stack, Fig. 7, one sees that the diamagnetic $(2,-1)$ level has an avoided crossing with the paramagnetic level $(4,-1)$ at 2.5 kG. Additionally, there is another such avoided crossing at 1.3 kG involving the paramagnetic $(4,-2)$ and the diamagnetic $(2,-2)$ levels. The avoided crossing at higher field is apparent in the theoretical work of Tinkham and Strandberg,[23] but the lower one is not. The Stern-Gerlach deflection shifts caused by these diamagnetic $\leftrightarrow$ paramagnetic interconversions again are dramatic, Fig. 7, with the lower anticrossing showing a rapid reversal of sign and the one at higher field reversing much less rapidly.

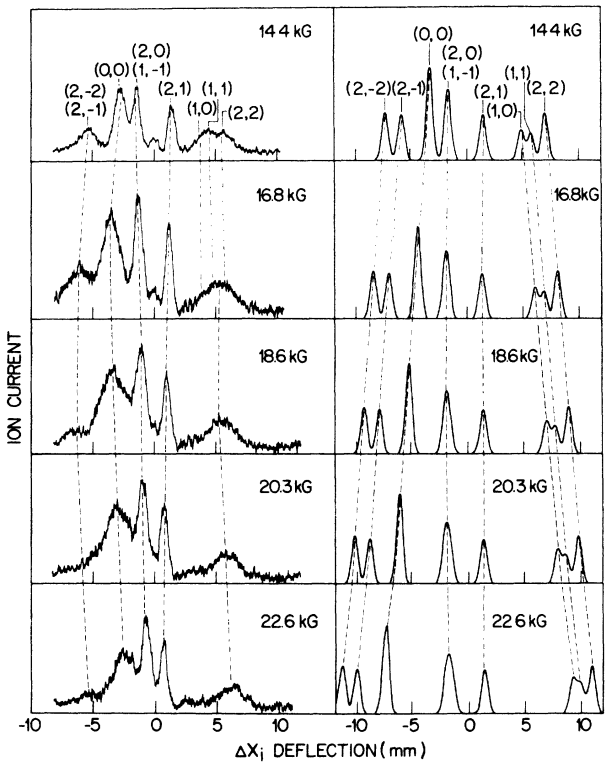


FIG. 6. *Left panel*: Stern-Gerlach deflection patterns measured for oxygen as a function of field strength $H_0$ (14.7–22.6 kG) in the sweet zone. The oxygen stagnation pressure was 2200 Torr and the nozzle diameter 300 $\mu$m. *Right panel*: Calculated magnetic deflection patterns for oxygen assuming a constant width for each component and thermal equilibrium among the zero-field levels $J=0$, $J=2$, and $J=1$ at 4 K. Levels are labeled as $(J,M_J)$.

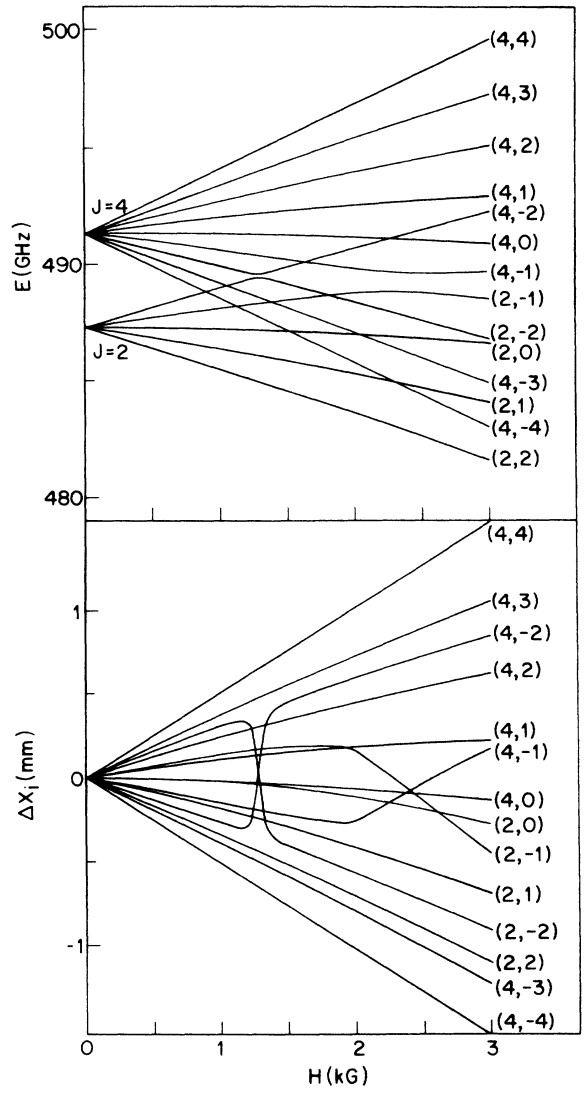


FIG. 7. *Upper panel*: Zeeman splitting calculated for the $K=3$, $J=2$ and $K=3$, $J=4$ manifold of $^{16}O_2$ at low fields. *Lower panel*: Calculated Stern-Gerlach displacements of the $K=3$, $J=2$ and $K=3$, $J=4$ levels showing paramagnetic $\leftrightarrow$ diamagnetic reversals at 1.3 and 2.5 kG.

### B. Deflections in high fields

Although our electromagnet is capable of generating a field of only 23 kG in the Stern-Gerlach experiment, the calculations are readily extended beyond that range and show several interesting features. Thus, not only do certain levels within $K=3$ show avoided crossing at low fields, but similar effects involving levels springing from manifolds of different $K$ are predicted at high fields. In Fig. 8, the Zeeman patterns calculated for $K=1$ and $K=3$ are plotted out to 105 kG. In the regime 20–70 kG, the Zeeman shifts are largely linear with field strength, with the levels nicely grouped as expected for Paschen-Back decoupling of momenta in the two states. However, in the vicinity of 80 kG, the (2,2), (1,1), and (1,0) diamagnetic components of $K=1$ have clear avoided crossings with, respectively, the (2,2), (2,1), and (2,0) paramagnetic components of $K=3$. The result of this $(K=1)$–$(K=3)$ interference in regard to the displacement of the $K=1$ levels is dramatic, Fig. 8. As the levels pass through the anticrossing region, the wave functions of the paramagnetic $(K=3)$ and diamagnetic $(K=1)$ species mix and eventually reverse character. Thus at $\sim$40 kG, the diamagnetic Paschen-Back levels of $K=1$ begin to reverse their displacements and in the process are again resolved. These displacements pass through $\Delta X_i=0$ at 80 kG, and then being paramagnetic at higher fields, they rapidly converge upon the displacements of the $(2,-2)$, $(2,-1)$ and (0,0) paramagnetic levels. The paramagnetic displacements of the levels transformed in the anticrossing equal those of the lowest paramagnetic levels, because both sets of levels at 90–105 kG have essentially the same $M_S$ values ($M_S=-1$) and the same Zeeman slopes, Fig. 8.

Conversely, the three paramagnetic levels of $K=3$ involved in the anticrossing become diamagnetic at fields above 80 kG, with displacements which converge upon those of the seven levels of $K=3$ which remain consistently diamagnetic. It is clear from the diagram, how-

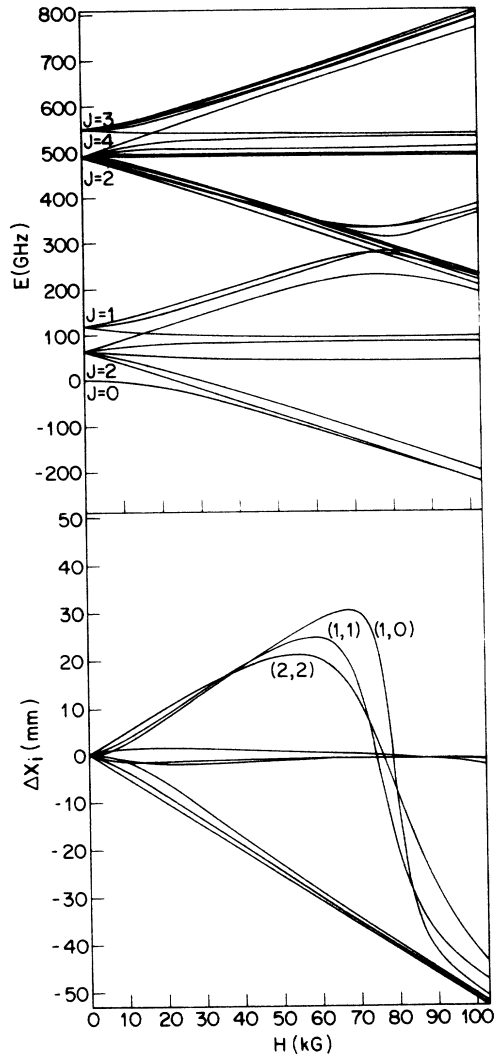


FIG. 8. *Upper panel*: Zeeman energy plots calculated for the $K=1$ ($J=0,2,1$) and $K=3$ ($J=2,4,3$) spin-rotational levels of $^{16}O_2$ out to 105 kG. Not all of the 21 $M_J$ levels of $K=3$ are resolved in this drawing. *Lower panel*: Stern-Gerlach deflection pattern calculated for the $K=1$ spin-rotational levels of $^{16}O_2$ out to 105 kG.

ever, that these three now diamagnetic levels will again switch their magnetic character as they attempt to traverse the nonmagnetic levels of the same $M_J$ values at about 500 GHz and 150 kG, Fig. 7.

## IV. RESULTS

### A. Comparison of theory and experiment

The Stern-Gerlach spectra predicted on the assumption of a homogeneous field gradient are compared with the experimental scans in Figs. 5 and 6. As can be seen there, remarkably good agreement exists between the predicted and observed deflection spectra for $0<H_0<12.6$ kG, as regards the number of levels, their separations, and their relative intensities. The $k_0^{\text{expt}}$ value mentioned in the preceeding ($1.85\times10^{-5}$ cm/MHz) was chosen so as to fit the observed deflection of the (2,2) level at 4 kG. The calculations give an unambiguous level assignment, as indicated in the figure, as well as a rotational temperature among the $J$ levels of $K=1$. In agreement with the assumption of equal *a priori* probabilities for the $M_J$ levels, the integrated intensities observed for the resolved deflections for $J=2$ molecules in the $(2,-2)$, $(2,-1)$, and (2,2) substates are essentially equal at fields up to 12.6 kG. Similarly, the integrated intensities of the resolved deflections for $J=1$ molecules in the (1,1) and (1,0) substates also are equal.

As good as the fit appears to be, there are three aspects of the comparison between theory and experiment which are troubling: (i) The appearance of a peak at $\Delta X_i=0$ in the experimental spectra determined at 9.8 and 12.6 kG (Fig. 5), whereas none is predicted at this position for the $K=1$ manifold; (ii) the calculation predicts that all peaks have equal widths, whereas this is not observed to be the case; and (iii) all peaks are predicted to shift monotonically to larger values of $\Delta X_i$ upon going from zero field to 22.6 kG, whereas at higher fields the peak deflections are observed to reverse direction somewhat and move to slightly *smaller* values of $\Delta X_i$. We consider each of these points in the following.

### B. Peak in the zero gap

There is disagreement between theory and experiment in the region $+1$ mm $<\Delta X_i<-1$ mm for $H_0$ between 9.8 and 18.6 kG, Figs. 5 and 6. Theory predicts that the deflections of molecules in the (2,0) and $(1,-1)$ states remain unresolved at $+1.0$ mm at 12.6 kG (as observed), and that there is no beam intensity at $\Delta X_i=0$. On the other hand, the experimental spectra at both 9.8 and 12.6 kG clearly show peaks in the zero gap. Working in a fixed geometry, Amirav and Navon[13] also report that 90% of the $O_2$ beam intensity is deflected off the center line at 10 kG, with 10% still remaining at $\Delta X_i=0$. As seen in Figs. 3 and 8, at the high-field Paschen-Back limit, three $(J,M_J)$ levels do regroup to form the $M_S=0$ level which will fall at $\Delta X_i=0$. However, 12.6 kG is far from this Paschen-Back situation. The problem would seem to rest either with the assumption that only $K=1$ is populated in our experiment, or with the assumption that all of the $O_2^+$ detected by the mass spectrometer came from the ionization of $O_2$.

In Fig. 9, the rotational temperature assumed in the calculation is increased step wise to 10 K to show how structure can arise from the $K=3$ manifold along with that from $K=1$ at 12.6 kG. In the case of $K=3$, of the 21 $M_J$ sublevels, (4,1) is sufficiently horizontal in the Zeeman diagram[23] as to remain virtually undeflected in the Stern-Gerlach spectrum. Thus if the temperature is sufficiently high, molecules in the (4,1) level of $K=3$ will appear in the zero gap of the $K=1$ deflection spectrum; all other bands involving $K=3$ levels at 10 K are overlapped by more intense deflections from $K=1$, except for a weak feature predicted to appear at $+3.0$ mm.

Note, however, that upon raising the rotational temperature from 4 (Fig. 5) to 10 K (Fig. 9), there is a pre-

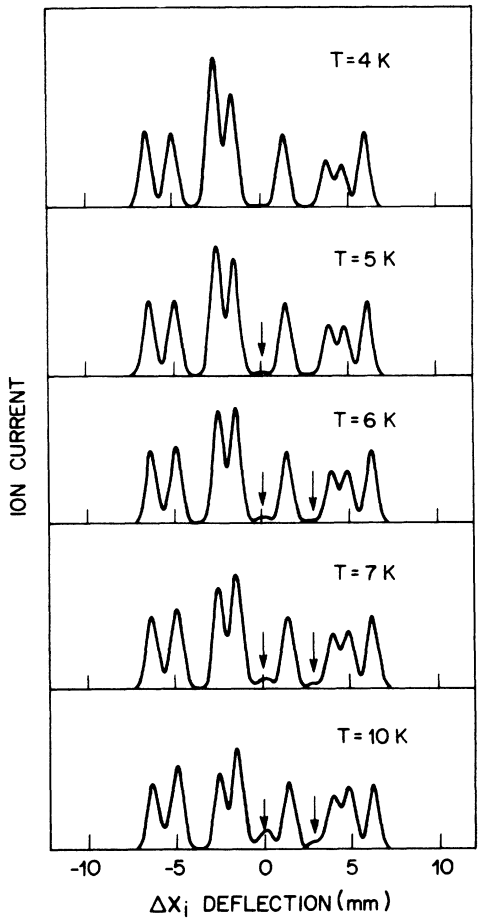


FIG. 9. Predicted deflection spectra as a function of the rotational temperature $T$ at a field $H_0=12.6$ kG. Arrows indicate the positions of bands due to population of $K=3$ levels.

dicted reversal of intensity ratios between the (0,0) band and the unresolved $(1,-1)$ and (2,0) bands, all within $K=1$. Since the observed ratio is that predicted at 4 K, we conclude that our beam is too cold to allow significant population of $K=3$ levels. A more likely explanation of the observed band at $\Delta X_i=0$ is that it is related to the high stagnation used in these experiments, which promotes cluster formation in the beam. In this situation, the peak at $\Delta X_i=0$ could result from the presence of diamagnetic $O_2$ clusters in the beam which are undeflected by the magnetic field, but which fragment to $O_2^+$ upon electron impact in the ionizer of the MS. Indeed, both $O_4^+$ and $O_6^+$ are detected in the pulsed beam, and each shows almost no deflection up to the highest field gradients. The Stern-Gerlach patterns of these species are discussed further in Sec. IV F.

### C. Theory of deflection peak bandwidths and shift reversals

A major discrepancy between experiment and the constant-force theory is evident in Figs. 4–6. As shown there, theory predicts that the displacements $\Delta X_i$ of all bands in the $K=1$ spectrum increase monotonically with increasing field up to 16 kG, and from that point on only those of the (2,1), $(1,-1)$ and (2,0) levels reverse direction. In contrast to this, the observed deflection of molecules in $(2,-2)$ is linear up to about 10 kG, but then actually reverses slightly at higher fields, Fig. 6. Almost all of the other levels behave similarly. This problem arises because the deflections were calculated in a field [Eq. (6)] of constant gradient at all positions inside the sweet zone, and in part because $\alpha_0$ so far has been assumed to be a constant, independent of the field $H_0$ as predicted by the two-wire model. Another consequence of the simple theory behind Eq. (6) is that the line shape of each peak is necessarily the same for a field of constant gradient, whereas the experimental peaks show varying widths. A more realistic approximation is to use Eq. (5) for the field, with $\beta$ nonzero.

We now develop a simple theoretical model based upon Eq. (5) which describes not only the shifted positions of peaks in the Stern-Gerlach deflection spectrum, but their variable widths as well. The initial distribution of molecules along the $x$ axis is denoted by $I(x)$, with characteristic half-width $\sigma_0$ around the center of the distribution at $x_0$. Molecules in state $i$ pass through the deflecting-field magnet in a time $t=l/v$, and then through a field-free region to reach the final detector-slit axis $X$ at time $T=L/v$ after leaving the magnet. The final deflected position $X_i$ is thus a function of the starting point $x$ of a given trajectory. The final distribution along the detector slit axis is denoted by $J_i(X)$, with a half-width $\sigma_i$, and is obtained by integrating over all trajectories leading to position $X$,

$$J_i(X)=N_i\int I(x)\delta(X-X_i)dx \ , \tag{10}$$

where again $N_i$ is the *a priori* Boltzmann probability of the molecular state. In the theory that follows, $X_i$ has a simple linear dependence on $x$, and because of the $\delta$-function normalization in Eq. (10), the ratio of final (deflected) and initial widths of a peak in the spectrum is given by

$$\sigma_i/\sigma_0=dX_i/dx \ . \tag{11}$$

Finally, for comparison with experiment, we consider a detector signal function

$$S(X)=\sum_i S_i(X) \tag{12}$$

summed over all occupied spin-rotational states. Here $S_i(X)$ is obtained by integrating $J_i(X)$ convoluted with a detector slit function $D(x')$, which has a half-width $\sigma_d$,

$$S_i(X)=\int J_i(X+x')D(x')dx' \ . \tag{13}$$

Although additional averaging over molecular velocities would be required in general, we assume here a single velocity $v$ characteristic of a high Mach value for the supersonic beam.

In order to apply the preceding distribution formulas, $X_i$ has to be expressed as a function of $x$. As a first approximation, which can be solved exactly, we consider a simple linear force field acting on the molecule as it

passes through the magnet gap. Expanding the force in powers of $x-x_0$ and retaining only the linear terms and constants, we have the classical equation of motion

$$m\ddot{x}=\alpha_0 F_0-\alpha_0^2 F_1(x-x_0)\ . \tag{14}$$

Here the constants $F_0$ and $F_1$ are obtained from derivatives of the adiabatic molecular Zeeman energy with respect to the magnetic field at $x_0$, with

$$F_0=H_0 dE_i/dH\ , \tag{15}$$

$$F_1=H_0^2 d^2E_i/dH^2+\beta H_0 dE_i/dH\ . \tag{16}$$

The magnetic field parameters $\alpha_0$ and $\beta_0$ are defined in Eqs. (3) and (4).

When $F_1=0$, Eq. (14) leads to the zeroth-order deflection formula [Eq. (6)] in Sec. IV C. When the force constant $F_1$ is positive, however, Eq. (14) describes simple harmonic motion of the molecule about the stable equilibrium position

$$x_m=x_0+F_0/\alpha_0 F_1 \tag{17}$$

with frequency

$$\omega=\alpha_0(F_1/m)^{1/2}\ . \tag{18}$$

One important consequence of this treatment is that the distribution of molecules in the positive $x$ direction tends to grow sharper, or undergo spatial focusing, as individual molecules move toward the stable energy minimum. On the other hand, when $F_1$ is negative, the position $x_m$ corresponds to an energy maximum, the frequency $\omega$ is imaginary, and the distribution tends to become broader. In general, both types of behavior can occur, depending upon the behavior of the possible values of $E_i$ at a given field $H_0$ at $x_0$.

After passing through the magnet gap, the molecules follow a straight-line trajectory which includes a velocity component in the $x$ direction. The exact solution for the final position $X_i$ is readily obtained, and may be cast into a form

$$X_i=x_0+\Delta X_i+(x-x_0)\sigma_i/\sigma_0\ , \tag{19}$$

which involves a simple linear dependence on the initial position $x$. The terms $\Delta X_i$ and $\sigma_i/\sigma_0$ represent the "shift" and the "reduced width" of the Stern-Gerlach "resonance" peaks in the spatial deflection spectrum. In this,

$$\Delta X_i=\alpha_0\gamma_i G F_0 \tag{20}$$

and

$$\sigma_i/\sigma_0=1-\alpha_0^2\gamma_i G F_1\ . \tag{21}$$

The factor $\gamma_i$ is most conveniently expressed in terms of the phase $Q=|\omega|l/v$ as

$$\gamma_i=\frac{l\left[\frac{\sin(Q/2)}{Q/2}\right]^2+2L\left[\frac{\sin Q}{Q}\right]}{l+2L},\quad F_1>0$$

$$\gamma_i=\frac{l\left[\frac{\sinh(Q/2)}{Q/2}\right]^2+2L\left[\frac{\sinh Q}{Q}\right]}{l+2L},\quad F_1<0 \tag{22}$$

$$\gamma_i=1,\quad F_1=0\ .$$

The shift formula, Eq. (20), is identical to Eq. (6) except for the scale factor $\gamma_i$, which tends to have values $\gamma_i<1$ when $F_1>0$, and $\gamma_i>1$ when $F_1<0$. In the present experimental setup, we find that $\gamma_i$ differs from unity by at most a few percent. The explicit dependence of $\gamma_i$ upon the experimental constants is thus illustrated by the following leading-order expression at small values of $Q$:

$$\gamma_i\simeq 1-(\alpha_0^2 l^2 F_1/12mv^2)\left[\frac{l+4L}{l+2L}\right]\ . \tag{23}$$

Given the functional form of $X_i$ in Eq. (19), we are now in a position to compute the final deflection functions $J_i(X)$ and $S_i(X)$. In order to illuminate their essential characteristics analytically, we shall consider a simple Gaussian model for both the initial distribution and detector slit functions,

$$I(x)=[1/\sigma_0(2\pi)^{1/2}]\exp\{-\tfrac{1}{2}[(x-x_0)/\sigma_0]^2\}\ , \tag{24}$$

$$D(x')=[1/\sigma_d(2\pi)^{1/2}]\exp[-\tfrac{1}{2}(x'/\sigma_d)^2]\ . \tag{25}$$

Substituting the preceding functions into Eqs. (10) and (13), we obtain the final distributions

$$J_i(X)=[N_i/\sigma_i(2\pi)^{1/2}]\times\exp\{-\tfrac{1}{2}[(X-x_0-\Delta X_i)/\sigma_i]^2\} \tag{26}$$

and

$$S_i(X)=[N_i/\Sigma_i(2\pi)^{1/2}]\times\exp\{-\tfrac{1}{2}[(X-x_0-\Delta X_i)/\Sigma_i]^2\}\ . \tag{27}$$

It is evident from Eq. (26) that $\Delta X_i$ and $\sigma_i$ do, in fact, control the shift and half-width of the deflection peak, as previously stated. The half-width parameter $\Sigma_i$ for the signal function $S_i(X)$ is determined from the combination rule

$$\Sigma_i^2=\sigma_i^2+\sigma_d^2 \tag{28}$$

for these Gaussian functions.[24] Note that Eq. (27), which includes a different $\Sigma_i$ for each state, reduces to the simpler function Eq. (9) with constant $\Sigma$, if $F_1$ is set equal to 0. In this case, $\sigma_i=\sigma_0$ from Eq. (21), and hence a constant value of $\Sigma_i=(\sigma_0^2+\sigma_d^2)^{1/2}$ is obtained from Eq. (28). Our earlier choice of $\Sigma=0.30$ mm to display deflection spectra is seen here to be consistent with a choice of parameters $\sigma_0=\sigma_d=0.21$ mm.

Figure 10 illustrates the field dependence of computed relative widths of peaks $(\sigma_i/\sigma_0)$ for the $K=1$ manifold of oxygen, assuming constant magnetic field parameters

$\alpha_0=3.10\ \text{cm}^{-1}$ and $\beta_0=1.15$ from the two-wire model, and $k_0^{\text{expt}}=1.85\times10^{-5}$ cm/MHz. The corresponding shifts $\Delta X_i$ are very similar to those of Fig. 4 since $\gamma_i$ equals approximately 1 over this range of fields. Note that the widths of peaks for the three diamagnetic states which are predicted to suffer positive $\Delta X_i$ deflections also are predicted to drop to zero below 10 kG. This spatial focusing is unique in that the widths of the other components either decrease somewhat, as with (2,1), or increase with increasing field, as with (1,−1), (2,0), (0,0), (2,−1), and (2,−2). This focusing manifests itself in the final distribution in Eq. (26) and (27) when $\sigma_i$ goes to zero, so that $J_i(X)$ approaches a δ-function spike and the signal function $S_i(X)$ reduces to the detector slit function as $\Sigma_i$ goes to $\sigma_d$. At higher fields, $\sigma_i$ becomes negative for these states, corresponding to the situation wherein the focussed beam has undergone a reflection through the center of the distribution. It is interesting to note as well how closely the predicted pattern of widths (Fig. 10) and deflections (Fig. 4) mirror one another, in the sense that within each group of three levels having the same general degree and sign of deflection, the general width behavior also is comparable. We are presently investigating the width of the (2,2) peak at 5.9 kG as a function of the detector slit width in order to test the prediction of extreme narrowing for this peak suggested by Fig. 10. Anderson *et al.*[25] previously have used the state-selective focusing properties of a hexapolar magnet field to separate the magnetic substates of NO $^2\Pi_{3/2}$.

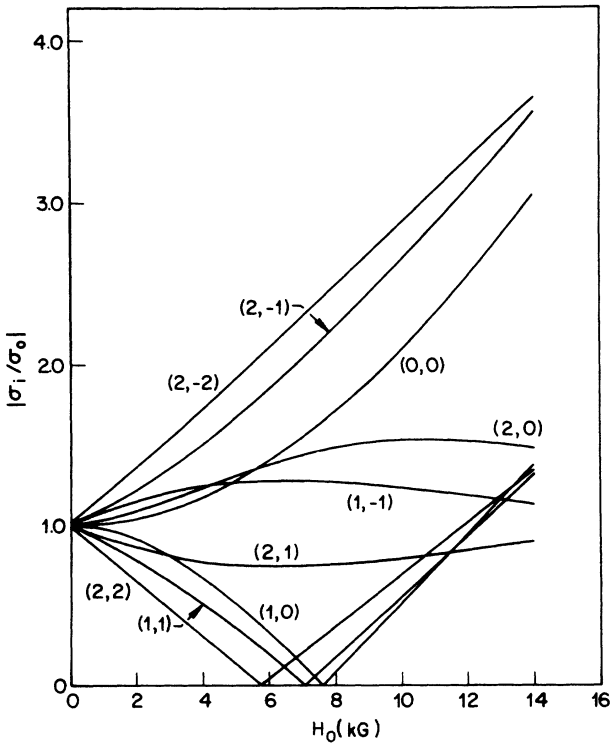


FIG. 10. Relative half-widths ($\sigma_i$) of the $K=1$ components of oxygen compared to the zero-field half-width ($\sigma_0$), computed with $\alpha=3.10\ \text{cm}^{-1}$, $\beta=1.15$, and $k_0^{\text{expt}}=1.85\times10^{-5}$ cm/MHz.

### D. Fitting of theory to experiment

Given the theory of the bandwidth as stated in the preceding, our goal in this section is to identify values of $G$, $H_{\text{expt}}$, $\alpha$, $\beta$, and $T$ (the rotational Boltzmann temperature), which can reproduce the salient features of the experimental deflection spectra when used with the linear force model.

Although it is possible to regard $G$ as an adjustable parameter in Eqs. (20) and (21), it is difficult to disentangle $G$ from the corresponding value of the parameter $\alpha_0$. We therefore regard $G$ as an apparatus constant, to be computed from Eq. (8). In the present apparatus, measured velocities of 750 and 816 m/s from two time-of-flight studies of nitrogen suggest a value of $v=733$ m/s for oxygen. This is consistent with estimates of the supersonic beam velocity provided by the relationship $mv^2/2=C_PT_0$ at high Mach values if it is assumed that the heat capacity $C_p$ equals $\frac{7}{2}k$ for oxygen, and that the stagnation temperature of the gas behind the valve, $T_0$, equals 295 K. With $l=5$ cm and $L=60$ cm, we obtain from Eq. (8) the value

$$G=0.723\times10^{-5}\ \text{cm}^2/\text{MHz}\ . \tag{29}$$

In our earlier attempt to fit the deflection spectra (see Fig. 4) it was assumed that the magnetic field at the center of the sweet zone ($H_0$) was identical to the experimentally measured field ($H_{\text{expt}}$). A more careful analysis of the relative spacings of peaks, however, suggests that $H_0$ is in fact slightly smaller than $H_{\text{expt}}$ in the current apparatus. The observed splitting patterns at $H_{\text{expt}}=5.9$, 9.8, and 12.6 kG, for example, are best described by the theory if we use fields of $H_0=4.8$, 8.7, and 11.8 kG, respectively. Reasons for this difference may include the possibility that $H_{\text{expt}}$ was measured closer to the convex pole tip, and/or that there possibly is a lower effective field at the ends of the magnet. However, the relationship between $H_0$ and $H_{\text{expt}}$ is not a simple scaling as would be expected from the two-wire model. One function which closely relates the two field values is

$$H_0=H_{\text{expt}}\{1+A\exp[-(H_{\text{expt}}/B)^2]\}^{-1}\ , \tag{30}$$

with $A=0.32$ and $B=10.1$ kG. Equation (30) reduces to $H_0=H_{\text{expt}}$ at high fields and $H_0=0.76H_{\text{expt}}$ at low fields. One consequence of using $H_0$ instead of $H_{\text{expt}}$ is that it brings low-field estimates of the field-gradient parameter $\alpha=k_0/G$ into closer agreement with the ideal value $\alpha_0=3.10\ \text{cm}^{-1}$ from the two-wire model. The splitting constant $k_0^{\text{expt}}=1.85\times10^{-5}$ cm/MHz used in Fig. 4, for example, was derived using values of $H_{\text{expt}}$ and yields $\alpha=2.56\ \text{cm}^{-1}$, about 18% below $\alpha_0$. The corresponding splitting constant for $H_0$ is

$$k_0=k_0^{\text{expt}}H_{\text{expt}}/H_0=2.44\times10^{-5}\ \text{cm/MHz}\ ,$$

with $\alpha=3.37\ \text{cm}^{-1}$, only 9% above $\alpha_0$. This agreement of course is subject to the experimental uncertainty in the apparatus constant $G$, which possibly may be as high as 15%.

The strategy for fitting the spectrum at each field is (1) determine $H_0$ from the splitting interval ratios or Eq.

TABLE I. Empirical parameters used in the linear force model.

| $H_{expt}$ (kG) | $H_0$ (kG) | $\bar{\alpha}$ | $\beta$ |
|---|---|---|---|
| 1.55 | 1.2 | 1.09 | 0 |
| 4.0 | 3.1 | 1.05 | 0 |
| 5.9 | 4.8 | 1.00 | 2.0 |
| 9.8 | 8.7 | 0.89 | 2.2 |
| 12.6 | 11.8 | 0.80 | 2.5 |
| 14.4 | 13.8 | 0.70 | 3.5 |
| 16.8 | 16.5 | 0.61 | 5 |
| 22.6 | 22.6 | 0.50 | 10 |

(30), (2) adjust the parameter $\alpha$ to fit the magnitude of the splitting, (3) adjust $\beta$ to fit the relative widths of the peaks, and (4) adjust $T$ to fit the relative heights of peaks. The empirically derived values of $\alpha$ are conveniently expressed in terms of the two-wire value $\alpha_0$ by means of the scale parameter $\bar{\alpha}=\alpha/\alpha_0$. Best-fit results for $H_0$, $\bar{\alpha}$, and $\beta$ as a function of $H_{expt}$ are listed in Table I.

The smaller values of $\bar{\alpha}$ at higher fields are necessary if the model is to account for the observed contraction of the experimental shifts. The corresponding increase in the width parameter $\beta$ reflects the general broadening of experimental peaks at higher fields, as well as counteracting the effect of smaller values of $\alpha$ in Eq. (21). These values of $\beta$ are intended to represent only the approximate magnitude of the parameter in this initial study. Nonetheless, they clearly demonstrate a marked deviation from the two-wire value $\beta_0=1.15$ even at low fields.

The deflection spectra as calculated using the best-fit parameters for each field (Table I) are shown in Fig. 11, for comparison with the experimental spectra of Figs. 5 and 6. Though the match still is not perfect, we see that the inclusion of the second derivative of the field along with variables $\alpha$ and $\beta$ now reproduces the pattern of exaggerated broadening of the bands at large $|\Delta X_i|$ and also tends to reverse the direction of the deflection of species having negative $\Delta X_i$, as observed. The largest differences between theory and experiment occur for the peaks with the largest deflections, at high fields, where additional broadening is expected as molecules move outside of the sweet zone of "constant" field gradient. This experimental broadening effect is *not* included in the linear force model, and so the empirical values of $\beta$ found here may in fact be artificially high due to this deficiency.

Another factor which must be considered here is the possibility of paramagnetic beam components leaving the sweet zone at high fields and colliding with the convex pole face PF1, Fig. 1, thereby altering a state's deflection amplitude and bandwidth. We estimate that this interference will occur first for $(2,-2)$, the level most strongly attracted to PF1, when the deflection inside the magnet gap reaches a value $\delta=-0.1a=-0.32$ mm. This corresponds to a critical deflection of

$$\Delta X^*=\delta(1+2L/l) \tag{31}$$

at the detector, or $\Delta X^*=-8$ mm in the present experiment. In the theoretical spectra, deflections of this magnitude begin at fields of about 14–16 kG. There are very few deflections greater than $-7$ mm in the experimental spectra even at the highest fields, presumably because of a lower effective value of $\alpha$. However, above 16 kG, the peak $(2,-2)$ at $-6$ mm tends to lose intensity, Fig. 6, and undergoes a greater reversal of deflection direction than its (2,2) counterpart at $+6$ mm. The (0,0) peak at $-3$ mm also exhibits a much larger reversal of direction. As collisions seem an unlikely explanation for reversal of the (0,0) peak, these results suggest the possibility of a greater asymmetry in the magnetic field as molecules approach the pole tip. In spite of these uncertainties, the overall agreement of the computed deflection spectra with the experimental spectra of Figs. 5 and 6 is satisfying.

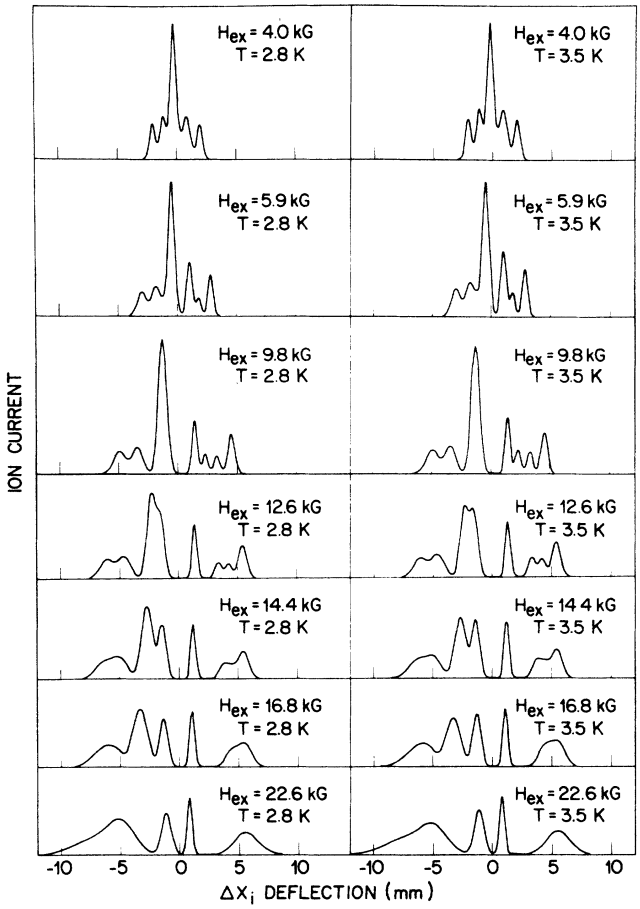


FIG. 11. Computed deflection spectra for oxygen using the field parameters given in Table I and rotational temperatures of 2.8 (left) and 3.5 K (right).

As a consequence of the variable widths of peaks in the linear-force model, the empirically determined rotational temperatures are now somewhat lower; the full range of computed spectra at 2.8 and 3.5 K are displayed in Fig. 11. Interestingly, the relative heights of the peaks in the 0 to $-4$ mm range at fields between 12 and 15 kG are very sensitive to rotational temperature. Our data at 14.4 kG are fit much better in this respect by $T=3.5$ K than $T=2.8$ K.

### E. Isotope effects

Because $^{16}O$ has no nuclear spin, the nuclear statistics in the $^{16}O_2$ molecule allow only rotational levels with $K$ odd, the lowest of which is $K=1$. On the other hand, if one or both of the $^{16}O$ nuclei is replaced by $^{17}O$ (spin $=\frac{5}{2}$), then the restriction on $K$ is relaxed and $K=0$ becomes the lowest rotational level. Having no rotational angular momentum, the $K=0$ level of $^{17}O_2$ is free of spin-rotational coupling, and so will have a Stern-Gerlach deflection spectrum which is very different from that of $^{16}O_2$ in $K=1$. Neglecting electron-nuclear hyperfine coupling, the deflection spectrum of $^3\Sigma_g^-$ $^{17}O_2$ in its $K=0$ state should consist of just three components, the second of which has $\Delta X_i=0$ at all fields. This stands in contrast to the pattern of nine levels appropriate to $K=1$, none of which falls at $\Delta X_i=0$ for magnetic fields between 5.9 and 23 kG. Actually, at a rotational temperature of a few degrees kelvin, both $K=0$ and $K=1$ levels of $^{17}O_2$ will be populated; however, the $^{16}O$-$^{17}O$ isotope effect in the overlapping deflection spectra will be most evident at $\Delta X_i=0$ ($5.9<H<23$ kG), where $K=0$ has a strong line and $K=1$ has none. As with $^{16}O$, the $^{18}O$ nucleus has zero spin; the lowest allowed rotational level in $^{18}O_2$ is $K=1$, and the deflection spectrum will closely resemble that of $^{16}O_2$.

Stern-Gerlach deflection spectra have been determined for an oxygen sample having 36 at. % $^{17}O$ and 64 at. % $^{18}O$. Due to the small amount of gas available to us, we were able to run only a few spectra before the stagnation pressure fell to unusably low levels. Nonetheless, reproducible spectra of modest quality were obtained with the mass spectrometer locked successively onto masses 34 ($^{17}O_2$), 35 ($^{17}O\,^{18}O$), and 36 ($^{18}O_2$) at a magnetic field of 12.6 kG. These spectra are displayed in Fig. 12 together with that of $^{16}O_2$ determined at a comparably low stagnation pressure. As can be seen there, the results are in agreement with our qualitative expectations. In both $^{17}O_2$ and $^{17}O^{18}O$ there is observed a prominent feature at $\Delta X_i=0$, whereas in $^{16}O_2$ and $^{18}O_2$, the corresponding region is free of deflected molecules. Though the (0,0) component of $K=0$ is obviously at $\Delta X_i=0$, the (0,1) and $(0,-1)$ components are not as easily found. Inspection of the deflection spectra of $^{17}O_2$ and $^{17}O^{18}O$ shows that relative to the peak at $\Delta X_i=-2$ mm in the spectra of $^{16}O_2$ and $^{18}O_2$, the spectra of the samples with nuclear spin have increased intensity in the vicinity of $\Delta X_i=-5$ to $-6$ mm. This is likely to be the location of the $(0,-1)$ paramagnetic component of $K=0$. The corresponding (0,1) diamagnetic component then would be expected at $\Delta X_i=5-6$ mm, where again there is intensity observed beyond that expected from the $K=1$ spectrum.

The qualitative assignment of the deflection spectrum of $^{17}O_2$ given in the preceding is totally confirmed by calculation of its spectrum, which places the three lines of the $K=0$ manifold at $-5.5$, 0, and $+4.8$ mm, assuming a beam velocity of 733 m/s, the field-free molecular constants appropriate to $^{16}O_2$, and a rotational temperature of 7.0 K.

One sees in these simple results yet another way in which the Stern-Gerlach deflections may be of use in the separation of isotopes. Amirav and co-workers[14–16] demonstrated how the Stern-Gerlach effect when combined with excitation of a radio-frequency resonance could be used to defocus a particular isotopomer of an atom or molecule. We see from the spectra in Fig. 12 that the isotopically sensitive microwave pumping is not necessary in those high-symmetry cases where the nuclear statistics lead to different rotational populations and thereby different deflection patterns. In the case of oxygen, the isotopomer containing one or two atoms of $^{17}O$ will have one-third of its intensity at $\Delta X_i=0$ at fields above 10 kG, whereas the isotopomers involving $^{16}O_2$ and/or $^{18}O_2$ will have no beam intensity at $\Delta X_i=0$ at the same fields.

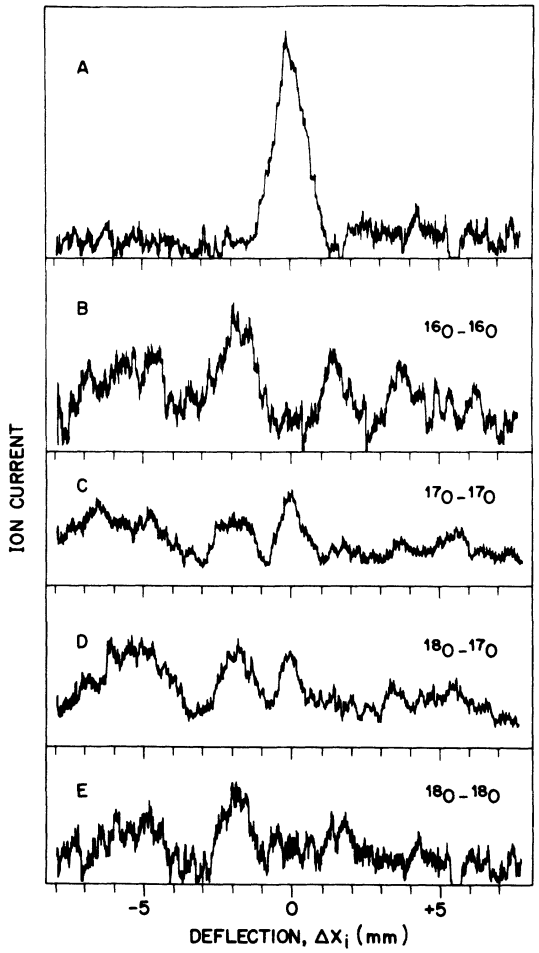


FIG. 12. Stern-Gerlach deflection spectra of the isotopomers of $O_2$ at a magnetic field of 1.55 kG (panel *A*) and at a field of 12.6 kG (panels *B*, *C*, *D*, and *E*). In each case, the stagnation pressure was in the range 250–600 Torr, which in the case of $^{16}O_2$ is sufficient to give cooling comparable to that achieved in Fig. 5.

### F. Oxygen clusters

To this point in the analysis, it has been assumed that the ionic species onto which the mass spectrometer has

been tuned was the parent ion of the neutral species deflected in the magnet gap. This is not necessarily so, as is well known to all who have tried to characterize neutral clustered species by electron-impact mass spectrometry. That is to say, the observed pattern of deflections which we have attributed to $O_2$ logically might have arisen from deflections of an $O_6$ cluster, for example, which then fragmented upon ionization to produce $O_2^+$. Of course, the fitting of the spectra using the molecular parameters of $O_2$ show that this is not the case for the spectra in Figs. 5 and 6 (except for the weak bands at $\Delta X_i = 0$). However, the same argument does not hold necessarily for spectra determined while monitoring $O_4^+$ or $O_6^+$.

Setting the mass spectrometer to detect $O_4^+$ or $O_6^+$ in beams generated at a stagnation pressure of 7000 Torr $^{16}O_2$ in each case gave peaks showing a small but definite shift and broadening to the paramagnetic side. However, we have been unable as yet to resolve any structure in these spectra. As we are not certain that the $O_4^+$ and $O_6^+$ ion signals necessarily correspond to $O_4$ and $O_6$ neutral-molecule deflections in the magnet, our conclusions that $O_4$ and $O_6$ are paramagnetic species is highly tentative. Working in a neon matrix Goodman and Brus[26] report $O_4$ to have a singlet ground state, whereas Van Deursen and Reuss,[27] mention that they too have determined the deflection spectrum of $O_4$ and that it is a paramagnetic species.

*Note added in proof.* We have just learned of the earlier work of Schnurmann [R. Schnurmann, Z. Phys. **85**, 212 (1933)], who also studied the Stern-Gerlach spectrum of $O_2$ in a molecular beam. Although he used an apparatus different from ours, the deflection spectra reported by him qualitatively resemble those calculated by us as appropriate to rotational temperatures of 200–300 K. As such, they show relatively little structure.

## ACKNOWLEDGMENT

We have benefited from extended discussions with Professor A. Amirav, Dr. S. Millman, and Dr. M. Mandich, and thank them for their interest in this work.

---

*Present address: Integrated Device Technology, Inc., 3236 Scott Blvd., Santa Clara, CA 95051.

†Present address: Department of Chemistry, Bar Ilan University, Ramat Gan, Israel.

[1]N. H. de V. Heathcote, *Nobel Prize Winners in Physics, 1901–1950* (Books for Libraries, Freeport, New York, 1971), p. 389.

[2]W. Gerlach and O. Stern, Ann. Phys. **74**, 673 (1924).

[3]W. Gerlach and O. Stern, Z. Phys. **9**, 349 (1922).

[4]W. Gerlach and O. Stern, Z. Phys. **9**, 353 (1922).

[5]W. Gerlach and O. Stern, Z. Phys. **8**, 110 (1922).

[6]O. Stern, Z. Phys. **7**, 249 (1921).

[7]D. M. Cox, D. J. Trevor, R. L. Whetten, E. A. Rohlfing, and A. Kaldor, J. Chem. Phys. **84**, 4651 (1986).

[8]W. D. Knight, Helv. Phys. Acta **56**, 521 (1983).

[9]W. D. Knight, R. Monot, E. R. Dietz, and A. R. George, Phys. Rev. Lett. **40**, 1324 (1978).

[10]D. M. Cox, D. J. Trevor, R. L. Whetten, E. A. Rohlfing, and A. Kaldor, Phys. Rev. B **32**, 7290 (1985).

[11]D. J. Meschi and A. W. Searcy, J. Chem. Phys. **51**, 5134 (1969).

[12]A. Amirav and G. Navon, Phys. Rev. Lett. **47**, 906 (1981).

[13]A. Amirav and G. Navon, Chem. Phys. **82**, 253 (1983).

[14]A. Amirav and U. Even, J. Appl. Phys. **51**, 1 (1980).

[15]A. Amirav and U. Even, Nucl. Instrum. Methods **205**, 579 (1983).

[16]A. Amirav, U. Even, and J. Jortner, J. Chem. Phys. **73**, 4217 (1980).

[17]J. B. M. Kellogg and S. Millman, Rev. Mod. Phys. **18**, 323 (1946).

[18]J. H. Van Vleck, *The Theory of Electric and Magnetic Susceptibilities* (Oxford, London, 1932), p. 262.

[19]A. Amirav, U. Even, and J. Jortner, Chem. Phys. **51**, 31 (1980).

[20]J. Mettes, B. Heijmen, J. Reuss, and D. C. Laine, Chem. Phys. **87**, 1 (1984).

[21]M. Tinkham and M. W. P. Strandberg, Phys. Rev. **97**, 937 (1955).

[22]M. Tinkham, Ph.D. thesis, Massachusetts Institute of Technology, 1954.

[23]M. Tinkham and M. W. P. Strandberg, Phys. Rev. **97**, 951 (1955).

[24]For comparison, a corresponding Lorentzian distribution model for $I(x)$ and $D(x')$ leads to Lorentzian distributions for $J_i(X)$ and $S_i(X)$ with half-widths $\sigma_i$ and $\Sigma_i$, respectively. The Lorentzian half-width combination rule is simply $\Sigma_i = \sigma_i + \sigma_d$.

[25]S. L. Anderson, P. R. Brooks, J. D. Fite, and O. Van Nguyen, J. Chem. Phys. **72**, 6521 (1980).

[26]J. Goodman and L. Brus, J. Chem. Phys. **67**, 4398 (1977); **67**, 4408 (1977).

[27]A. Van Deursen and J. Reuss, Int. J. Mass Spectrom. Ion Phys. **23**, 109 (1977).